Supporting Information

Yeh et al. 10.1073/pnas.0907406106

SI Text

Simple Receptive Fields Were Found in All Layers of V1. Fig. S1 shows the modulation ratio (f1/f0) for the 205 single units recorded from different layers of V1. Among the 38 simple cells (f1/f0 ≥ 1), 29 of them (76%) had significant subspace receptive fields. Most of the 29 simple cells with significant subspace receptive fields (93%, $n = 27$) had receptive fields with multiple segregated on and off subregions (Fig. S1*B*). As can be seen in Fig. S1*A*, such cells with high modulation ratio (f1/f0) and high SNR were found in output layers of V1 including layer 2/3 and layers 5 and 6 and in layer 4C. Five example cells that had high f1/f0 SNR are numbered and plotted as red outlined circles in Fig. S1*A* to show that such simple cells could be found in every layer of V1. Fig. S1*B* displays the subspace maps for these neurons from 40 to 100 ms and their spatial variance vs. time plots.

Interestingly, 31% ($n = 52/167$) of complex cells (f1/f0 < 1) also had mappable Hartley maps, and 79% of the Hartley-mappable complex cells ($n = 41/52$) had receptive fields with multiple segregated on and off subregions. The majority of the Hartley-mappable complex cells (71%, $n = 37/52$) had unimodal or unmappable receptive fields when mapped with sparse noise.

Over the entire V1 population of cells mappable with Hartley stimuli, the modulation ratio (f1/f0) and SNR were weakly correlated for subspace maps ($r = 0.29$, $P = 0.01$) but uncorrelated for sparse-noise maps ($r = 0.05$, $P = 0.63$; Fig. S1 *C–E*). The average SNR of subspace maps was significantly larger for simple cells than for complex cells (simple: 4.46 ± 2.71, complex: 3.21 ± 2.77, $P = 0.0003$, Wilcoxon rank sum test), but the average SNR for sparse-noise maps was not significantly different between simple and complex cells (simple: 5.02 ± 3.54, complex: 4.90 ± 7.08, $P = 0.18$, Wilcoxon rank sum test). Furthermore, 60% ($n = 124/205$) of our V1 population did not have mappable Hartley maps (SNR < 1.8), and the majority of them (93%, $n = 115/124$) were categorized as complex (f1/f0 < 1). The unmappable cells and their mappable counterparts had comparable mean firing rates to Hartley stimuli (mappable: 7.33 ± 7.92 spikes per s; unmappable: 7.91 ± 8.80 spikes per s, $P = 0.29$, Wilcoxon rank sum test). Therefore, their unmappability was not caused by low responsiveness to visual stimuli.

Surgery and Preparation. Acute experiments were performed on adult Old World monkeys (*M. fascicularis*). All surgical and experimental procedures were performed in accordance with the guidelines of the U.S. Department of Agriculture and had been approved by the University Animal Welfare Committee at the New York University. Animals were sedated with midazolam (0.3 mg per kg, i.m.) and anesthetized initially with ketamine (30 mg per kg, intramuscular) and then with isofluorane (1.5–3.5% in air) after being intubated. After i.v. catheters were placed in both hindlimbs, the animal was placed in a stereotaxic frame and maintained on opioid anesthetic (sufentanil citrate, 6–12 μg per kg h^{-1}, i.v.) during the craniotomy. A craniotomy (≈5 × 7 mm) was made in one hemisphere posterior to the lunate sulcus (≈15 mm anterior to the occipital ridge, ≈10 mm lateral from the midline). A small opening in the dura (≈3 × 5 mm) was made to provide access for multiple electrodes. After surgery, anesthesia was maintained with a continuous infusion of sufentanil citrate (6–12 μg per kg·h^{-1}, i.v.), and the animal was paralyzed with pancuronium bromide (0.1 mg per kg·h^{-1}, i.v.) and maintained hydrated by giving fluid at a rate of ≈6 mL per kg·h^{-1} (the rate was adjusted hourly to keep the urine-specific gravity within normal range (≈1.010 g/mL)). Vital signs, including heart rate, electroencephalogram, blood pressure, and oxygen level in blood were closely monitored throughout the experiment. Expired carbon dioxide was maintained close to 32–38 mmHg, and rectal temperature was kept at a constant 37 °C with the use of a feedback-controlled heating pad. A broad spectrum antibiotic (Bicillin, 50,000 units per kg, i.m.) and antiinflammatory steroid (dexamethasone, 0.5 mg per kg, i.m.) were given on the first day and every 24 h during the experiment. The eyes were treated with 1% atropine sulfate solution to dilate the pupils and with a topical antibiotic (gentamicin sulfate, 3%) before being covered with gas-permeable contact lenses. Foveae were mapped onto a tangent screen with a reversing ophthalmoscope. The visual receptive fields of isolated neurons were later mapped on the same tangent screen, keeping reference to the foveae. Proper refraction was achieved by placing corrective lenses in front of the eyes on custom-designed lens holders. The eyes were stabilized with ophthalmic rings to minimize drift of visual field position.

Electrophysiological Recordings and Data Acquisition. A matrix of seven independently moveable electrodes (Thomas Recording) was used to record simultaneously from multiple cortical cells in V1. The seven electrodes were arranged in a straight line with each electrode separated from its neighbor by ≈300 μm. The electrode consists of a platinum/tungsten core (25 μm in diameter and 1 μm at the tip) covered with an outer quartz-glass shank (80 μm in diameter), and has an impedance value of 1–4 MΩ. The multielectrode matrix was precisely positioned before recordings so the tip of the matrix was ≈3 mm above the cortical surface. We first placed the tips of all seven electrodes near the cortical surface and then advanced them in ≈100-μm steps. This setup allowed simultaneous recordings of multiple neurons within the same cortical layer, all at similar visual eccentricities. Electrical signals from the seven electrodes were amplified, digitized, and filtered (0.3–7,500 Hz) with a preamplifier (Tucker-Davis Technologies; model number RA16SD) configured for multichannel recording. The Tucker-Davis system was interfaced to a computer (Dell) running a multichannel version of the OPEQ program (designed by J. A. Henrie, New York University, New York) to acquire both spike and local field potential data. Spike waveforms were inspected online during the experiment and were again carefully verified offline using custom spike-sorting software (designed by D.X.). Strict criteria for single units included fixed shape of the action potential, the absence of spikes during the absolute refractory period, and a well-isolated cluster from principal components analysis. Visual stimuli were generated with the custom OPEQ program running in a Linux computer (Dell) with a graphics card with Open GL optimization. Data collection was synchronized with the screen refresh to a precision of <0.01 ms. Stimuli were displayed on a 20-in monitor (IIyama HM 204DTA flat color graphic display; pixels: 1024 × 768; frame rate: 100 Hz; mean luminance: 59.1 cd/m^2) with the screen viewing distance of ≈114 cm. The basic attributes of each cell were estimated by using small drifting sinusoidal gratings surrounded by gray background (both the gratings and the gray background had a mean luminance of 59.1 cd/m^2).

Receptive Field Mapping. We used both Hartley subspace stimuli (1) and sparse noise (2) to estimate spatiotemporal receptive fields of V1 neurons. The subspace stimuli were derived from a low-pass subset of the 2D Hartley functions that consisted of an orthogonal set of stationary sinusoidal gratings (2.4° × 2.4°) with

evenly spaced orientations, spatial phases ($n = 4$), and spatial frequencies (0.6–8.0 cycles/° in visual angle). Each subspace image appeared for 20 ms and the entire sequence lasted ≈15 min (a total of 1,052 images, each image presented ≈42 times). The sparse noise consisted of a sequence of randomly positioned (in a 12 × 12 sample grid) dark and bright squares (0.2° × 0.2°) against a gray background (luminance: 59.1 cd/m^2). The luminance of bright and dark squares was adjusted so the contrasts from the light increment (luminance: 107.3 cd/m^2) and light decrement (luminance: 11.1 cd/m^2) were nearly equal. Each sparse noise image appeared for 40 or 50 ms and the entire sequence lasted ≈14 or 18 min (a total of 288 images, each image presented 72 times). The subspace stimuli and the sparse noise were presented sequentially and the centers of both stimuli were kept the same and carefully positioned to allow simultaneous mappings of receptive fields of multiple neurons recorded from different electrodes.

Calculations of SNR and RFS. We used the SNR of the Hartley subspace map to determine whether or not a cell had a mappable receptive field. To define the SNR, we calculated the spatial variance of the map as $\sigma^2_{xy}(\tau) = \langle [R(x, y, \tau) - \langle R(x, y, \tau)\rangle]^2\rangle_{x,y}$ at different time delays (3), and then defined the peak time as the time delay when the spatial variance reached its maximum (τ_{peak}; see Fig. 1). The SNR was then calculated as the average variance within the peak 40 ms (from τ_{peak} −20 ms to τ_{peak} +20 ms; the yellow region in Fig. 1*C*) divided by the spatial variance at time 0 (see Fig. 1*C*). In a total of 205 V1 cells, 81 had Hartley SNR ≥ 1.8 and were the mappable neurons used for the analyses in this study. The receptive-field map at the peak time was chosen to represent the spatial properties of a mappable cell.

We then calculated a RFS to quantify how similar Hartley and sparse-noise maps were. Because the number of pixels between Hartley maps (128 × 128 pixels) and sparse-noise maps (12 × 12 pixels) differed significantly, the Hartley maps first were smoothed (with an 8 × 8 window) and then down-sampled to 16 × 16-pixel maps. Then both Hartley and sparse-noise maps were resized through bicubic interpolation (Matlab imresize function) to have 48 × 48 pixels. The spatial similarity index was then calculated as the pixel-by-pixel correlation coefficient between the Hartley map and the sparse-noise map (see Eq. **1** and refs. 4 and 5).

Note that the RFS was calculated by fixing the Hartley subspace map and moving the sparse-noise map along both x and y axes (± 24 of 48 pixels in either direction) to find the x, y position at which spatial correlation reached its maximum. When shifting the sparse-noise map, the pixels that fell outside of the fixed Hartley map were circularly rotated to the opposite side of the sparse-noise map so that all correlations were calculated for the same number of pixels. We took the maximum spatial correlation of the shift-corrected RFS to represent the spatial similarity of two maps. This step was critical because we were interested in similarity of two spatial structures. A small offset in receptive field centers, possibly caused by small eye movements between mappings, could degrade the apparent spatial similarity (see Fig. S1 *A* and *B* for simulations showing that the spatial similarity index decreased greatly even for a small displacement of two identical receptive fields). Indeed, the estimated similarity index RFS was significantly lower for all but two layer 4C cells ($n = 23$) when the two maps were directly cross-correlated without shifting (Fig. S1*C*; unshifted: ⟨RFS⟩ = 0.28 ± 0.32; shift corrected: ⟨RFS⟩ = 0.58 ± 0.22, $P < 0.0001$, Wilcoxon signed rank test).

Gabor Function Fitting for Estimating Preferred Orientation and Subregions. The subspace map and the sparse-noise map were fitted with 2D Gabor functions (6, 7) to extract spatial map parameters including the preferred-orientation axis and the number of subregions. The following is the 2D Gabor function:

$$h(x', y') = \exp((-(x'/\sqrt{2}\sigma_{x'})^2 - y'/\sqrt{2}\sigma)^2)\cos(2\pi f x' + \phi), \quad [2]$$

where (x', y') is obtained by translating the original coordinate system by (x', y') and rotating it by θ

$$x' = (x - x_0)\cos\theta + (y - y_0)\sin\theta \quad [3]$$

$$y' = (x - x_0)\sin\theta + (y - y_0)\cos\theta. \quad [4]$$

In this coordinate system, the cosine function in the Gabor varies only along the x' axis, and the two axes of the Gaussian envelope align with the x' axis (orthogonal orientation) and y' axis (preferred orientation), respectively. The θ is the preferred orientation. A subregion was considered significant if the maximum response within the subregion was >20% of the peak response across the entire spatial map (8). The goodness of fit (R^2) was not significantly different between sparse-noise maps and subspace maps for the same neurons ($P = 0.44$, Wilcoxon signed rank test), and the median goodness of fit was equal to 0.73 for both stimulus conditions.

Histology. Cells were assigned to different layers of V1 based on the results of track reconstruction (9–11). Along each track, we recorded the depths of every recording site during the experiment, and then made 3–4 electrolytic lesions at 600- to 900-μm intervals at the end of the experiment. A lesion was made by passing a 3-μA direct current for 2 s through the quartz platinum/tungsten microelectrodes (Thomas Recording) with a stimulus generator (ALA Scientific Instruments; model number STG-1001). After euthanasia, the animal was perfused through the heart with 1 L of heparinized saline (0.01M PBS) followed by 2–3 L of fixative (4% paraformaldehyde, 0.25% glutaraldehyde in 0.1 M phosphate buffer). After the brain was blocked and sectioned at 50 μm, the lesions were initially located in unstained sections and then the lesion sections were stained for cytochrome oxidase. Cytochrome oxidase provides good anatomical localization of the laminar boundaries. Cortical layers were determined based on the cell density and cytochrome oxidase-specific labeling (12). Fig. 1*A* shows an example of a 50-μm cytochrome-oxidase-stained slice with multiple lesions (indicated by arrows) made along 2 recording tracks. After locating the lesions within the sections, we reconstructed the electrode penetration by using a camera lucida and determined the location of each recorded site relative to the reference lesions and the layers of the cortex. The mean thickness of each layer was then used to determine each cell's normalized cortical depth ranging from 0 (representing the surface) to 1 (representing the boundary between layer 6 and the white matter). The assignment of cells to layers is crucial because the cortical connectivity of different layers in the primate cortex is very different and important for their function (13, 14).

Overall, we recorded from a total of 327 sites from four adult Old World monkeys. Among them 205 were verified as single units with offline spike sorting and had mean firing rate >1 spike per s in response to both subspace stimuli and sparse noise. We used drifting sinusoidal gratings (contrast: 99%; spatial frequency: 2 cycles/°; temporal frequency: 4 cycles/s; duration: 4 s) to measure the preferred orientation and the modulation ratio (f1/f0) of V1 neurons. The gratings were presented at 12–18 different directions. We found ≈40% of the 205 neurons and ≈52% of layer 4C neurons were unoriented based on the orthogonal/preferred orientation ratio (>0.5), a conventional measure of orientation selectivity. These results were consistent with several previous studies in monkey V1

(10, 11, 15). The 205 cells were categorized as simple (f1/f0 $\geq$ 1) or complex (f1/f0 $<$ 1) based the responses to optimally oriented gratings (16). Note that we used relatively large-sized patches of gratings (radius = 1.5–2° in visual angle) to cover the receptive fields of multiple cells recorded simultaneously with the multielectrode matrix.

1. Ringach DL, Sapiro G, Shapley R (1997) A subspace reverse-correlation technique for the study of visual neurons. *Vision Res* 37:2455–2464.
2. Jones JP, Palmer LA (1987) The two-dimensional spatial structure of simple receptive fields in cat striate cortex. *J Neurophysiol* 58:1187–1211.
3. Malone BJ, Kumar VR, Ringach DL (2007) Dynamics of receptive field size in primary visual cortex. *J Neurophysiol* 97:407–414.
4. David SV, Vinje WE, Gallant JL (2004) Natural stimulus statistics alter the receptive field structure of v1 neurons. *J Neurosci* 24:6991–7006.
5. Victor JD, Mechler F, Repucci MA, Purpura KP, Sharpee T (2006) Responses of V1 neurons to two-dimensional hermite functions. *J Neurophysiol* 95:379–400.
6. Jones JP, Palmer LA (1987) An evaluation of the two-dimensional Gabor filter model of simple receptive fields in cat striate cortex. *J Neurophysiol* 58:1233–1258.
7. Ringach DL (2002) Spatial structure and symmetry of simple-cell receptive fields in macaque primary visual cortex. *J Neurophysiol* 88:455–463.
8. Alonso JM, Usrey WM, Reid RC (2001) Rules of connectivity between geniculate cells and simple cells in cat primary visual cortex. *J Neurosci* 21:4002–4015.
9. Hawken MJ, Parker AJ, Lund JS (1988) Laminar organization and contrast sensitivity of direction-selective cells in the striate cortex of the Old World monkey. *J Neurosci* 8:3541–3548.
10. Ringach DL, Shapley RM, Hawken MJ (2002) Orientation selectivity in macaque V1: Diversity and laminar dependence. *J Neurosci* 22:5639–5651.
11. Blasdel GG, Fitzpatrick D (1984) Physiological organization of layer 4 in macaque striate cortex. *J Neurosci* 4:880–895.
12. Wong-Riley M (1979) Columnar cortico-cortical interconnections within the visual system of the squirrel and macaque monkeys. *Brain Res* 162:201–217.
13. Lund JS (1988) Anatomical organization of macaque monkey striate visual cortex. *Annu Rev Neurosci* 11:253–288.
14. Rockland KS, Lund JS (1983) Intrinsic laminar lattice connections in primate visual cortex. *J Comp Neurol* 216:303–318.
15. Hubel DH, Wiesel TN (1968) Receptive fields and functional architecture of monkey striate cortex. *J Physiol (London)* 195:215–243.
16. Skottun BC, et al. (1991) Classifying simple and complex cells on the basis of response modulation. *Vision Res* 31:1079–1086.

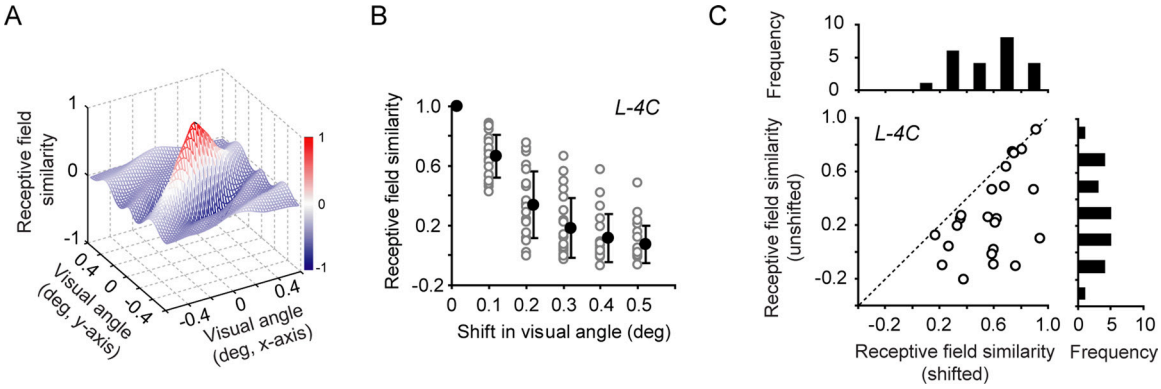

Fig. S1. RFS corrected by shifting. (*A*) A simulation of 2D cross-correlogram between two identical Hartley maps from an example layer 4C simple cell (Fig. 2*A Left*). We fixed one map and shifted the other identical map in both *x* and *y* axes (in 0.05° steps of visual angle) to calculate the pixel-by-pixel correlation coefficient and from that to calculate the receptive field similarity (as in Eq. **1**). (*B*) The RFS largely degrades even with a small displacement between two identical Hartley maps. Open circles represent the average correlation coefficient corresponding to the size of shifting in all directions for individual cells, and the filled circles indicate the average (± SD) of the 23 layer 4C cells with mappable Hartley maps. The similarity decreased 34% with a 0.1° shift and 66% with a 0.2° shift. (*C*) To correct for possible eye movements, we calculate the maximum spatial correlation as the RFS (see *Methods* for details). The scatter plot is RFS unshifted vs. RFS shifted for the 23 layer 4C cells. If there were no relative movement between measurements of the Hartley and sparse-noise maps, the RFS estimates should fall on the unity diagonal. Deviations from the diagonal indicate that the true RFS had to be obtained after shifting.

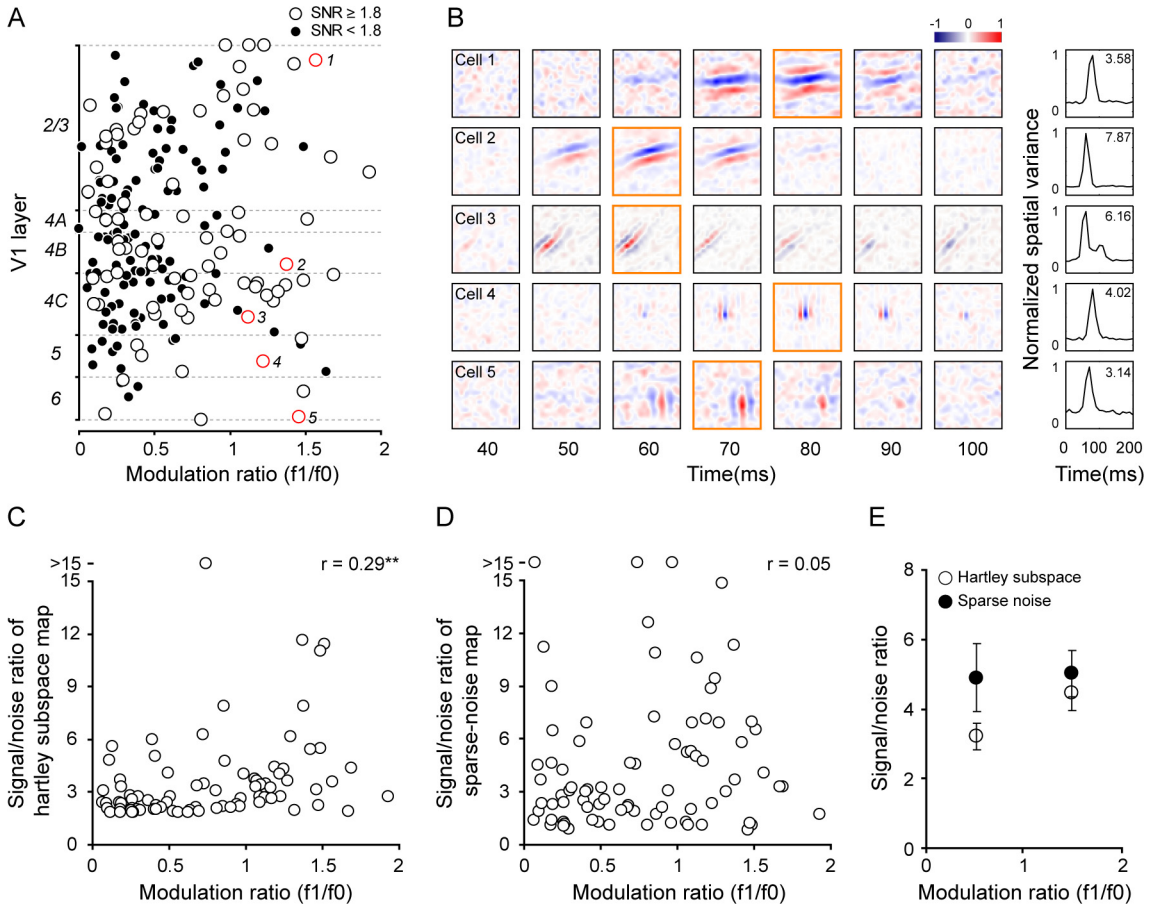

Fig. S2. Simple cells with mappable receptive fields were found in all layers of V1. (*A*) Mappable cells (○) and unmappable cells (●) with Hartley stimuli plotted verses relative V1 depth. (*B*) Spatiotemporal receptive fields (40–100 ms) and response time courses (last column) of 5 example cells from different layers of V1 (represented as red open circles with corresponding numbers in *A*). All five cells had Hartley subspace maps with segregated on and off subregions and had modulation ratios (f1/f0 ≥ 1) that would have them to be classified as simple. The number in the upright corner of the response time course is the SNR. (*C*) The SNR and the modulation ratio (f1/f0) are correlated for cells with mappable Hartley maps. (*D*) For cells with mappable Hartley maps, the SNRs from their sparse-noise maps were not correlated with the modulation ratios (f1/f0). (*E*) The SNRs of Hartley maps were significantly higher for simple cells than for complex cells. However, this was not the case for sparse-noise maps.